Quantifying modulation in the acoustic field of a small-scale rotor using bispectral analysisg

Baars, W.J.; Bullard , Liam; Mohamed, Abdulghani

DOI
10.2514/6.2021-0713

Publication date
2021

Document Version
Final published version

Published in
AIAA Scitech 2021 Forum

AIAA SciTech Forum
11–15 & 19–21 January 2021, VIRTUAL EVENT
AIAA Scitech 2021 Forum

10.2514/6.2021-0713

Quantifying modulation in the acoustic field of a small-scale rotor using bispectral analysis

Woutijn J. Baars*
Faculty of Aerospace Engineering, Delft University of Technology, 2629 HS Delft, Netherlands
Liam Bullard† and Abdulghani Mohamed‡
School of Engineering, RMIT University, Melbourne, VIC 3001, Australia

This paper describes a methodology to quantify inter-frequency modulation in the acoustic field of a small-scale rotor. How the blade passing frequency modulates the intensity of the higher-frequency (broadband) noise content is of specific interest, as this modulation is a major factor in the human perception of rotor noise from advanced air mobility vehicles and drones. A proposed modulation-parameter is based on post-processing steps that are applicable to a single acoustic time series. First, an auto-bispectral analysis assesses the dominant nonlinear, quadratic inter-frequency coupling between the blade passing frequency and the higher-frequency noise content. Secondly, the degree of modulation is determined using a robust parameter: a correlation parameter between the (low-frequency) modulating BPF signal and an envelope of the (higher-frequency) carrier signal. Provided that a single parameter is obtained for a given acoustic time series, the directivity pattern of the modulation strength can be inferred from data available from standard acoustic measurement campaigns. For illustration, an 11 inch diameter single-rotor in hover is considered, with acoustic data taken at 420 microphone positions within a plane perpendicular to the rotor disk. It is revealed that modulation is confined to a sector $\theta \approx (10^\circ, -45^\circ)$, where $\theta = 0^\circ$ is the rotor plane and negative angles are in the direction of the rotor-induced flow. The strongest modulation appears around $\theta \approx -15^\circ$. This work aids in quantifying the phenomenological description of modulation, namely that it results from the periodic advance and retreat of certain rotor blade's noise sources, relative to a stationary observer.

I. Introduction and context

Propulsion systems of advanced air mobility concepts, including urban air mobility (UAM) and drone-based applications, employ a multitude of rotors that are, by themselves, much smaller than the single-rotor technology of conventional helicopters. For instance, the many electrical takeoff and landing (eVTOL) prototype vehicles under development (examples in Fig. 1) comprise more than four—relatively small-scale—rotors. Assessing the rotor noise of new advanced air mobililty vehicles has gained a high priority, given that these vehicles are envisioned to operate in densily populated areas.[1] In this regard, engineering studies on the noise impact of small-scale rotors should be extended to include psycho-acoustic factors of human perception and annoyance.

A noise level that complies with a certification standard is not necessarily acceptable to the public, especially when advanced air mobility concepts come online, causing a growth in the number of rotorcraft operations in densely populated areas. At the moment, noise certification regulations fall short in addressing the human perception of an acoustic pressure time series. For instance, for helicopter noise certification per the 14 CFR Part 36 standard, both the tone-corrected (effective) perceived noise level (EPNL) and the A-weighted sound exposure level (SEL) do not characterize time-varying aspects of a noise signature. Moreover, according to the FAA, extending the EPNL metric with factors of human annoyance is not yet intended for the certification of advanced air mobility vehicles. There is however a growing awareness

*Assistant Professor, AIAA Senior Member, w.j.baars@tudelft.nl
†Ph.D. Candidate, liam.bullard@rmit.edu.au
‡Senior Lecturer, abdulghani.mohamed@rmit.edu.au

Figure 1. Various eVTOL vehicles that have been under development in recent years. Many of the advanced air mobility concepts include open rotor propulsion technologies; a wide variety of multi-rotor layouts exists among different designs. Photo credits from left-to-right: AirSpaceX, Volocopter and Hyundai/Uber.

that time-varying properties of the noise (an amplitude modulation), and its impulsiveness/sharpness are highly relevant for the level of annoyance;[2–7] this is in line with the conclusions made in the community of psycho-acoustics.[8] Most studies on acoustic aspects of small-scale rotors consider standard characterization schemes that rely on time/ensemble-averaging:[9–16] acoustic results are condensed to a set of acoustic spectra, their integrated energy (overall sound pressure level), as well as the directivity patterns of that (frequency-dependent) energy. Occasionally, studies do employ time-preserving schemes (wavelet transforms yielding time-frequency spectra), as those are required when dealing with non-stationary acoustic signals of flyovers and maneuvering systems.[17,18] As described in § I.B, we here extend the standard acoustic characterization by way of proposing a parameter that preserves characteristics of the time-varying amplitude of the high-frequency noise within a signal. This time-varying amplitude is known as the a modulation of rotor noise and occurs for all single- and multi-rotor configurations: *e.g.* the time-dependent *whooshing* of the noise from slowly rotating wind turbine-rotors, or the higher-frequency *buzzing* type of noise from drone propellers.

A. Modulation of open rotor noise

A great number of studies have addressed low-frequency noise modulation of wind turbines,[19–22] but to date, only a few studies have focused on rotor noise modulation in the context of aerospace vehicles.[23] When focusing on open rotors,[24–26] the main components of periodic noise are classified as thickness noise and blade loading or lift noise. In addition, broadband noise arises from turbulent flow over the blades, and vortical motions shedding turbulence past the trailing edge and blade-tip. The *total* noise of open rotors is a summation of the harmonic and broadband noise components and is conveniently assessed in the frequency domain. The frequency-dependent level of the perceived noise can vary with time, either due to a variation of inflow conditions on the rotating blade, or a periodic advance and retreat of the rotor blade's noise sources, relative to a stationary observer. These harmonic variations of the acoustic intensities (due to the varying source-receiver distance) and characteristic frequencies (via the Doppler effect) are dubbed amplitude and frequency modulations, respectively. In this work we refer to this phenomenon as *blade passing frequency modulation* (BPF modulation), as the main driver is the rotating motion of the blade. Note that the modulation time-scale is thus prescribed by the BPF; this is different from when a rotorcraft system, as a whole, moves relative to an observer. For the latter scenario the amplitude and frequency variations of the noise appear at the time scale of the flyover maneuver (this large time-scale modulation is absent as we focus on a stationary-positioned rotor system).

B. Present contribution and outline

Even though the working principle of BPF modulation is understood by realizing the harmonic variation in the source-receiver distance and a potential periodic fluctuation of noise source levels, a method to unambiguously quantify the degree of modulation requires attention. The aim of this paper is therefore:

> **To present a methodology for quantifying modulation in the acoustic field generated by a propulsive rotor, via post-processing steps applied to a collection of acoustic pressure time series. Here the modulation is driven by the periodic advance and retreat of the rotor blade's noise sources at a rate that is equal to the BPF.**

A synoptic outline of the paper is now provided. A central facet of this work is the use of benchmark acoustic data in the acoustic near- and far-fields of a small-scale rotor in hover. These data contain all noise field

characteristics of (small-scale) rotors in hover.[27] Descriptions of the experimental acquisition and data are provided in § II and § III, respectively. Subsequently, § IV describes the methodology for capturing the BPF modulation, resulting in a single parameter, for a given acoustic signal. Spatial trends of the modulation parameter within the acoustic field of the rotor are covered in § V.

With this work we aim to contribute to a more comprehensive quantification of the annoyance and human perception of rotorcraft noise. Rizzi *et al.*[28] outlined various goals to address barriers associated with UAM noise, one being: *"Define measurement methods/procedures to support noise regulations and assessment of community noise impact, and coordinate with UAM vehicle manufacturers on development of low noise approach and takeoff procedures for piloted and automated operations."* In this regard, a preliminary listening experiment indicated that the proposed modulation parameter is well-correlated with the degree of time-variation of the amplitude. Future work is needed to correlate this engineering parameter to human perception via psycho-acoustic methods. Once this parameter deemed viable in assessing aspects of annoyance, it can facilitate the assessment of the noise impact (by for instance applying it to data of high-fidelity numerical computations of rotor noise[29,30] or even to noise data of complete UAM vehicles in urban environments[31,32]). A modulation parameter can also form a cost function in a design optimization for low-noise rotor technologies. Such optimization exercises are of particular importance when considering integrated systems that are prone to stronger harmonic acoustic interference, such as stacked coaxial rotors.[33–35] Moreover, multirotor systems have the potential to influence the BPF modulation by way of controling the relative phase between the rotors.[36] Finally, BPF modulation aspects are critical for achieving realistic auralizations of rotorcraft noise,[37] and likewise, BPF modulation characteristics will benefit future extensions of noise prediction tools.[38–41]

II. Benchmark experiment of rotor noise

A. Experimental setup and acquisition

Facility. Acoustic measurements of a small-scale rotor in hover were carried out in an ETS Lindgren acoustic anechoic chamber at the CSIRO in Clayton, VIC, Australia (ISO 3745 certified). This fully-anechoic chamber has a sound absorption coefficient greater than 99% above 80 Hz and encompasses a suspended floor, acoustic absorber wedges and 200 mm thick acoustic wall, floor and ceiling panels. Internal dimensions are roughly 4.4 m (L) × 4.4 m (W) × 4 m (H).

Rotor test stand. A custom-built rotor test stand supported the small-scale rotor in hover. An RCbenchmark Series 1585 thrust stand provided a base for the motor-rotor assembly with thrust and torque measurement capabilities. The available ranges of measured thrust and torque were $F_z \in (-5, 5)$ kgf (with a tolerance $< 0.5\,\% \pm 0.001$ kgf) and $\tau \in (-1.5, 1.5)$ Nm (with a tolerance $< 0.5\,\% \pm 0.001$ Nm). A SUNNYSKY X2820 1100KV brushless motor was used and contained 14 rotor poles. A tachometer reading using a TCRT1000 reflective optical sensor gave a one-per-revolution signal of the motor casing for an accurate reading of the rotor's rotation speed and blade position. The induced flow direction was downward to prioritize clean inflow conditions to the rotor. The rotor was located in the center of the anechoic test environment, to ensure that any flow recirculation in the anechoic chamber—possibly affecting higher harmonic noise[42]—would be symmetric. The rotor disk was located four rotor diameters above the suspended floor to minimize ground effects. Note that all other clearances (sideline and upstream regimes) were much larger.

Propeller. The off-the-shelf rotor from APC Propellers (model 11x10e) has a diameter of $D_p = 2R = 0.2794$ m (11 inch), a mean pitch of 10 inch, and is considered an industry standard for small-scale unmanned aerial vehicles (UAVs), like the Skywalker X8. The thrust at cruise for a Skywalker X8 is approximately 1 kgf and is therefore taken as the nominal thrust set-point (§ II.B). A schematic of the test stand with nomenclature is provided in Fig. 2a.

Acoustic array. Acoustic data were acquired using microphones in the vertical plane perpendicular to the rotor disk.[a] A total of 30 microphones were mounted to a vertical boom using ~ 300 mm long rods (microphones were oriented such that their measuring diaphragms were co-planar with the measurement plane). This vertical boom was mounted to a linear traversing stage that could move the boom along

[a]This orientation avoids having to point the normal vector of the diaphragm to the sound source (its location is ambiguous for an aeroacoustic sound source[43,44]), but does require a correction for the grazing orientation, related to the intrusive nature and form factor of the microphone (90° incidence waves). This free-field microphone correction was applied in all spectral analysis, although it only slightly affects the amplitude at $f > 10$ kHz.

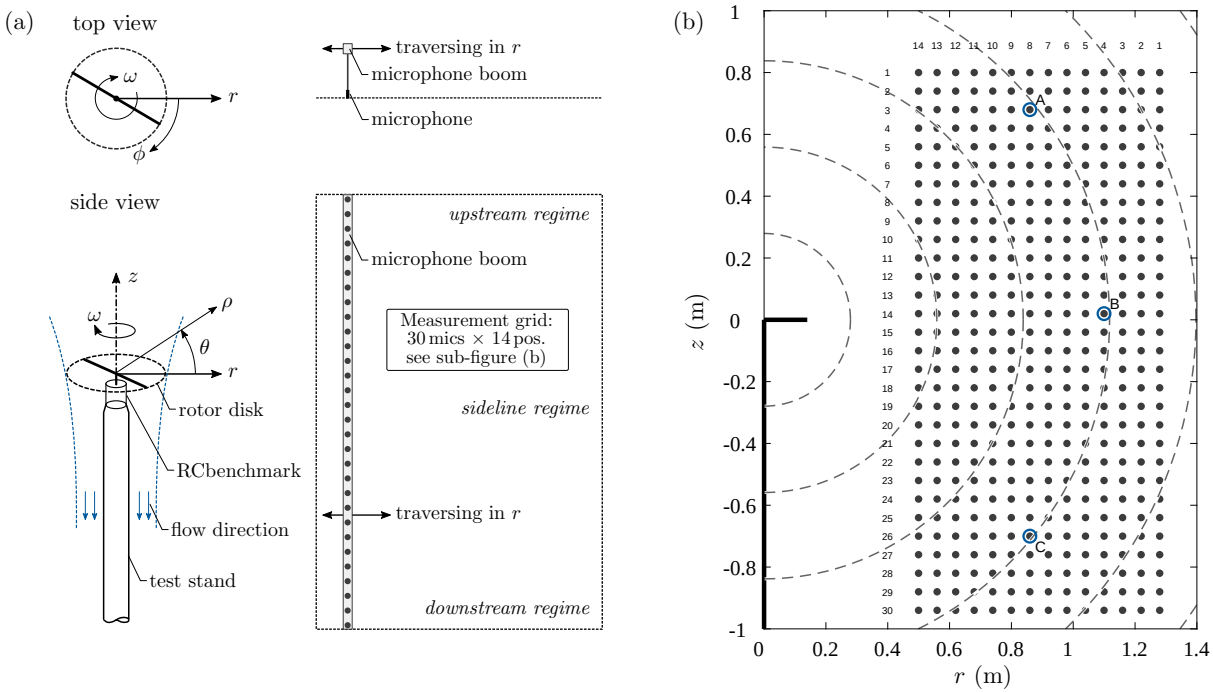

Figure 2. (a) Schematic of the experimental setup; coordinate system comprises axial coordinate z (being the rotor axis) and radial coordinate r; the rotor hub is located at $(z, r) = (0, 0)$. (b) Microphone positions (420 mapped out in total) in the (z, r) plane, at which acoustic pressure time series are available; grey-dashed arcs visualize one-rotor-diameter increments from the rotor hub. Positions A, B and C are used throughout this paper and are situated at $\rho \approx 4D_p$ at an angle of $\theta = 38.3°$, $\theta = 1.0°$ and $\theta = -39.2°$, respectively.

the radial direction. The acoustic field was mapped out by translating the boom to 14 radial positions; traversing steps of 60 mm equaled the equidistant microphone spacing along the vertical boom. Thus, in total, $30 \times 14 = 420$ pressure time series $p(z, r; t)$ were acquired and are situated in the near- and far-fields of the rotor (Fig. 2b). For reference, this study[45] employed a similar linear microphone array to map out the noise signature in the very near-field of a small-scale rotor.

The sensors used were G.R.A.S. IEPE type 40PH, 1/4 inch microphones with a frequency response range of 50 Hz to 20 kHz (±2 dB accuracy, with ±1 dB accuracy up to 5 kHz) and with a dynamic range of 32 dBA to 135 dB, with a sensitivity of 50 mV/Pa. Microphones were calibrated in situ with a B&K type 4230 piston-phone calibrator. All 30 microphones were IEPE powered by, and simultaneously sampled with, an LMS (Siemens) SCADAS Mobile SCM05 system. Acquisition was performed with on-board filtering prior to digitization with a 24-bit accuracy. All signals (including the tachometer signal) were sampled at $f_s = 102.4$ kHz for an uninterrupted duration of $T = 30$ seconds for each microphone-boom position (the sensor's natural frequency roll-off acted as a filter). The acquisition length of each time series equated to $2T\omega \approx 6679$ blade passages (for the 2-bladed propeller spinning at $\omega = 111.3$ rev/s); this was confirmed to be more than sufficient for converged bispectral statistics[46] at the lowest frequencies of interest (see § IV.A).

For spectral analysis, the one-sided spectrum is taken as $\phi_{pp}(z, r; f) = 2\langle P(z, r; f) P^*(z, r; f)\rangle$, where $P(z, r; f) = \mathcal{F}[p(z, r; t)]$ is the temporal FFT. Acoustic spectra are presented as the sound pressure level (SPL) in dB, following $\mathrm{SPL}(z, r; f) = 10 \log_{10}(\phi_{pp}(z, r; f)/p_{\mathrm{ref}}^2)$ with $p_{\mathrm{ref}} = 20$ µPa. Ensemble averaging was conducted using FFT partitions of $N = 16 f_s/\omega$ samples, to ensure that the discrete frequencies align with the BPF and its harmonics; this reduces the leakage of energy into frequencies neighboring the tones. This value of N gives a spectral resolution of $\mathrm{d}f = 6.95$ Hz and 419 ensembles with 50 % overlap.

B. Rotor operating condition

Operating conditions of the rotor are listed in Table 1. Atmospheric pressure, temperature and relative humidity of the test environment were measured as $p_\infty = 101\,600$ Pa, $T_\infty = 293.1$ K and RH = 60.1 %, respectively, yielding a density of $\rho = 1.207\,\mathrm{kg/m^3}$ and a sound speed of $a_\infty = 343.2$ m/s. The propeller

rotated at a constant rate of $\omega = 111.3\,\text{rev/s}$ (6679 RPM), resulting in a BPF of $f_b = 222.6\,\text{Hz}$. The tip Mach number was $M_{\text{tip}} \equiv 2\pi\omega R/a_\infty = 0.285$. A Reynolds number of $Re_{c75} \equiv c_{75}2\pi\omega 0.75R/\nu = 8.0 \cdot 10^4$, based on the blade chord of $c_{75} \approx 165\,\text{mm}$ at a radial position of $0.75R$, indicates that the propeller operates with a reduced efficiency,[47] and predicting the noise can be difficult.[27,48] Hence, the acoustic data can support simulation validation-type of studies.

Table 1. Rotor operating conditions of the APC 11x10e propeller in hover at 6679 RPM.

Operating regime				Performance					
ω (rev/s)	f_b (Hz)	M_{tip}	Re_{c75}	F_z (kgf)	τ (Nm)	P (W)	C_T	C_τ	FM
111.3	222.6	0.285	$8.0 \cdot 10^4$	1.014	0.169	118.2	$1.41 \cdot 10^{-2}$	$1.71 \cdot 10^{-3}$	0.690

In terms of aerodynamic performance, the rotation rate ensured a thrust of $F_z = 1.014\,\text{kgf}$ (close to our nominal set-point of 1 kgf) with a reaction torque of the motor-rotor assembly of $\tau = 0.169\,\text{Nm}$. Coefficients of thrust (C_T) and torque (C_τ), and the figure of merit (FM), were calculated via:

$$C_T = \frac{F_z}{\rho A\,(2\pi\omega R)^2}, \qquad C_\tau = \frac{\tau}{\rho A\,(2\pi\omega R)^2\,R}, \qquad \text{FM} = \frac{C_T^{3/2}}{\sqrt{2}C_P}. \tag{1}$$

Here $A = \pi R^2$ is the rotor disk area and power coefficient C_P is equal to C_τ. Rotor power in Watts is taken as $P = 2\pi\omega\tau$. Values of the performance parameters are listed in Table 1. The absolute thrust and torque, as well as the FM, agree well with a parametric study on small-scale propellers.[14] The thrust and torque coefficients are $\sim 20\,\%$ higher than the study by Tinney & Sirohi[14] (unobstructed wake) and may be caused by a small blockage effect of the rotor test stand in the wake, as well as by the larger propeller-pitch (10 versus 4.5 inch). Deviations in thrust (3 %) and torque (33 %), from the manufacturer's performance data, are attributed to simplifications in the theoretical predictions used to generate those data.

III. Acoustic field characteristics

A. Ensemble-averaged, and frequency-integrated, sound pressure level statistics

Acoustic spectra of the pressure time series at position B (indicated in Fig. 2b) are shown in Fig. 3a and support a description of the steps taken in all of our spectral analysis. That is, the spectrum of the

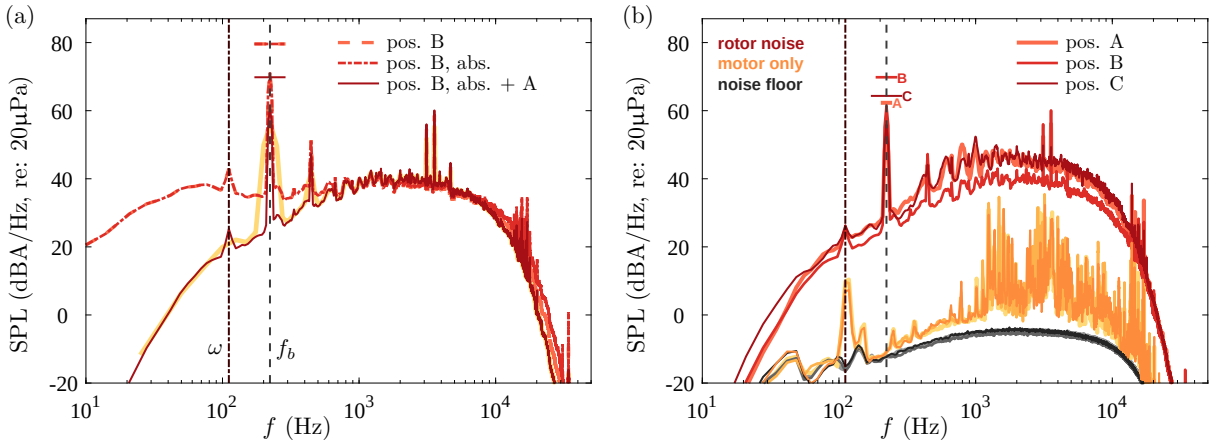

Figure 3. (a) Acoustic spectra at position B (see Fig. 2b): created from the raw acoustic time series (dashed), with a correction for atmospheric absorption (dash-dotted) and an additional A-weighting (solid). SPL magnitudes of the BPF peaks are indicated with horizontal bars and correspond to the amplitude of a pure tone at $f = f_b$ (see text). (b) Acoustic spectra at positions A, B and C (corrected for atm. absorption and A-weighted). Spectra of the motor-only noise (same ω) and the chamber's noise floor are also shown.

raw pressure time series was subject to a bandpass filter, with a flat response between 60 Hz and 15 kHz, suppressing the the non-anechoic, low-frequency content and the energy beyond the upper frequency range of

the microphone. The spectrum was also corrected for atmospheric absorption with an assumed propagation distance from the rotor hub (see[49] and ANSI S1.26-1996), meaning that the corrected spectrum represents the noise in the case of no absorption (primarily affecting $f > 10\,\mathrm{kHz}$). In addition, an A-weighting was applied (see[49] and ANSI S1.6-1967) to account for the relative loudness[50] perceived by the human ear; this weighting mainly attenuates the energy at frequencies below $2f_b$. Spectra in Fig. 3b, for positions A, B and C, show that the rotor noise magnitude is much larger than the noise floor of the sensors/chamber, and the noise of only the spinning motor (without propeller, but at the same RPM). The motor noise alone has the expected spectral peak at $f = \omega$ and includes a more broadband energy content at $f \in (1, 10)\,\mathrm{kHz}$. This latter component of noise, in the vicinity of $f = 14\omega$, is caused by the 14 magnetic poles of the motor (note that the motor noise is also known to arise from structural vibrations and harmonic interference[51,52]).

The SPL amplitudes of the BPF spectral peaks at $f = f_b$ are indicated with *horizontal bars*; that is, their magnitudes correspond to the rms-amplitudes of pure tones, being $A/\sqrt{2}$ for a harmonic wave with amplitude A. Hereby it is ensured that the magnitude is independent of the chosen spectral resolution $\mathrm{d}f$. Practically speaking, the amplitude is obtained via $\mathrm{SPL}(z, r; f = f_b) = 10\log_{10}(\phi_{pp}(z, r; f)\mathrm{d}f/p^2_{\mathrm{ref}})$ (note that ϕ_{pp} in dBA/Hz is premultiplied by $\mathrm{d}f$, to obtain the BPF peak amplitude in dBA). Note that the spectra generally include the noise field characteristics of small-scale rotors in hover.[9–14] However, the BPF higher harmonics are less pronounced than in some of the other data. Stephenson and coworkers[33,42] suggested that flow recirculation in a closed chamber can increase the magnitude of BPF harmonics (in line with other studies[53]). With our test set-up comprising a rotor-wall clearance of at least $\sim 8D_p$ to all sides (except for the ground plane at $\sim 4D_p$ clearance), this flow recirculation effect may be minor with, as a consequency, a lower-magnitude higher harmonic noise content (*e.g.* Fig. 4 of Stephenson *et al.*[42]) in comparison to other studies conducted with more confined setups. This explanation is speculative for the time-being, as no flow measurements were performed.

Provided that the aforementioned spectral analysis can be applied to each of the acquired acoustic time series, a spatial topography of the overall sound pressure level (OASPL), here denoted as $\overline{p}$, can be generated (Fig. 4a). Here $\overline{p}$ follows an integration of the rotor noise spectra in dBA. The OASPL $\overline{p}$ is the resultant of

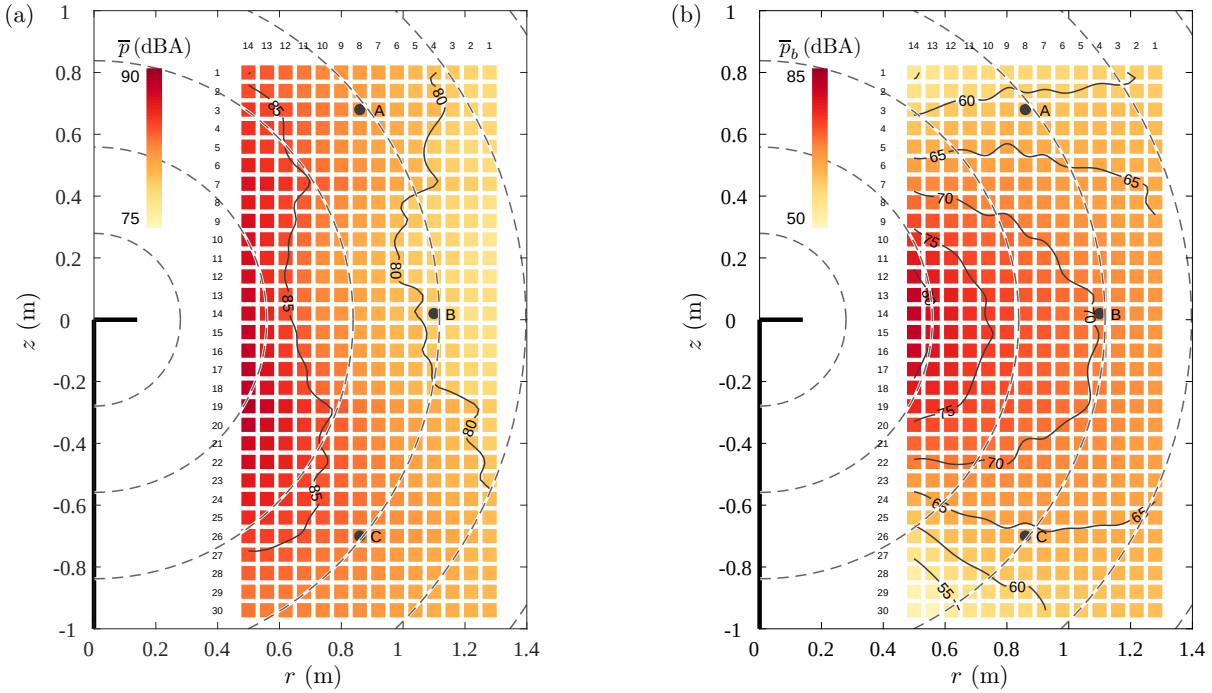

Figure 4. (a) Spatial field of the OASPL in dBA, following an integration of the rotor noise spectra (like the ones in Fig. 3b at positions A, B and C). (b) Spatial field of the BPF spectral peak amplitude in dBA, taken as the magnitude of a pure tone that is independent of the spectral resolution (see text).

thickness and loading noise components, and the superimposed broadband noise content.[24,54] The thickness noise, as well as the loading noise from thrust and torque, classifies primarily as a dipole source and its

radiated noise is most strongly confined to a region around the plane of the rotor disk. Since this periodic noise is strongly tied to the BPF, we illustrate this in Fig. 4b by visualizing the SPL magnitude of the BPF spectral peak (computed per the discussion above on the SPL magnitudes at $f = f_b$). The BPF noise directivity has a lobe-intensity that is oriented slightly towards the downstream region (as would be the case for a thrust-producing propeller). To further assess the directivity, $\overline{p}$ and $\overline{p}_b$ of all 420 measurement points are projected to a rotor-hub-centered arc of radius $\rho = 4D_p$[b], by assuming a spherical spreading law ($p \propto 1/\rho$) (when these data collapse on a single profile they were all taken in the acoustic far-field). Results for $\overline{p}$ and $\overline{p}_b$ are shown in Figs. 5a and 5b, respectively. In addition, Fig. 5c plots the integrated SPL for the frequency range $f > 5f_b$, and thus contains the noise in the absence of the BPF tone and its first few harmonics.

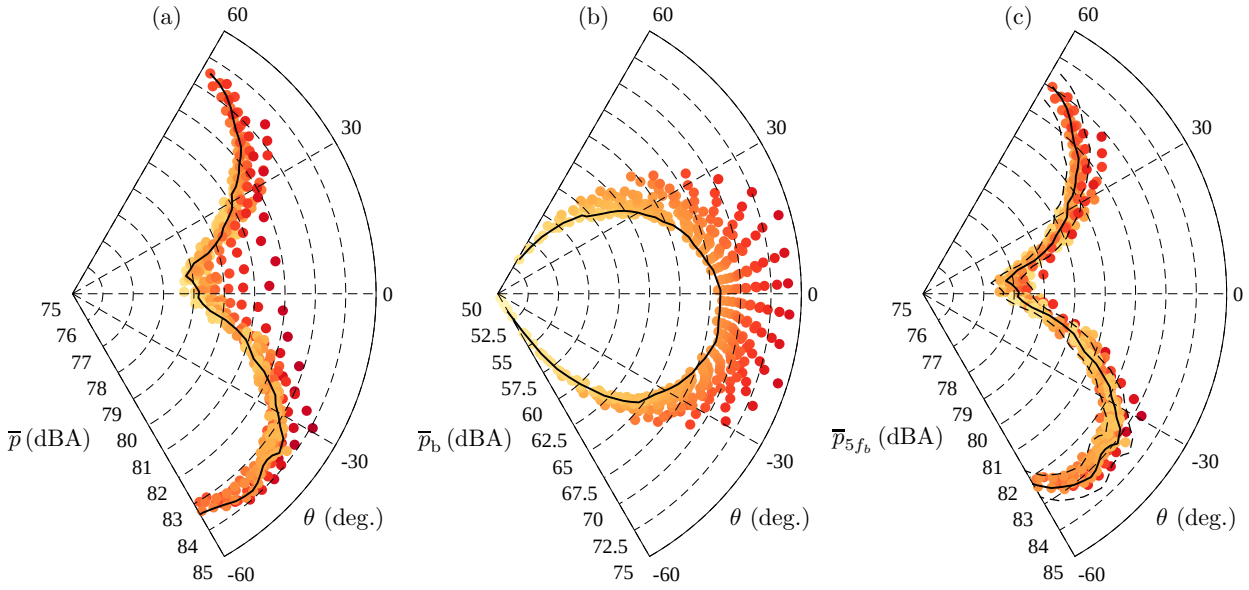

Figure 5. Noise directivity patterns obtained by projecting the data of all 420 measurement points to a rotor-hub-centered arc of radius $\rho = 4D_p$, via spherical spreading ($p \propto 1/\rho$). Data are (a) the OASPL $\overline{p}$, (b) the BPF spectral peak amplitude $\overline{p}_b$, and (c) the integrated SPL $\overline{p}_{5f_b}$ over the frequency range $f > 5f_b$. All data points are colored following the original (unprojected) magnitude of the noise (thus following Fig. 4); the black fitting line is formed by utilizing only the data points along the top, right and bottom perimeter of the grid.

The absence of a collapse in the data of $\overline{p}_b$ (Fig. 5b) suggests that the corresponding locations lay *not* within the acoustic far-field (for when the BPF spectral peak amplitude is concerned). That is, the data originating from positions closest to the source have dBA levels that are larger than those that would be obtained from following spherical spreading inwards, starting from the data points furthest out (those furthest data points along the top, right and bottom perimeter of the grid were used to form the black fit line). Given that the points close to the rotor obey a pressure decay that is steeper than per spherical spreading, it can be concluded that the BPF signature includes an hydrodynamic component (an *evanescent pressure wave*). Since our measurements extend to $\sim 5D_p$, we recommend to go at least beyond that for proper far-field measurements of rotor-BPF tones. The BPF noise not obeying far-field characteristics is the primary cause for the absence of collapse in the $\overline{p}$ data (Fig. 5a), since the higher-frequency content ($f > 5f_b$) shows an excellent collapse in Fig. 5c, to within ± 0.5 dBA as indicated by the dashed lines. The latter suggests that the sources emitting noise at $f > f_b$ are compact,[45] and that even the first point along $\theta = 0°$ is already in the far-field for those frequencies. That data point is located at $r = 1.79D_p$, or $r = 1.62(\lambda_b/5)$, with wavelength $\lambda_b = a_\infty/f_b$. Note that the modulation analysis of § IV is unaffected by the pressure decay obeying (or not obeying) far-field trends, as the modulation parameter is correlation-based and thus energy-normalized.

[b]Since the noise is, on-average, emitted from the center location of the spinning rotor, this hub-centered source position resulted in the best collapse of the data in Fig. 5.

B. Phase-averaged sound pressure level statistics

Moving towards acoustic modulation in rotor noise data, it is instructive to visualize phase-averaged pressure data. Phase-averaged data is denoted as $\widetilde{p}(z, r; \phi)$, where ϕ is the angular position of the blade. For $\phi = 0$, the spatial topography of $\widetilde{p}$ is shown in Fig. 6a (for the the raw pressure signal) and in Fig. 6b (with the BPF tone removed). It is evident that the acoustic waves emanate from a characteristic source close to

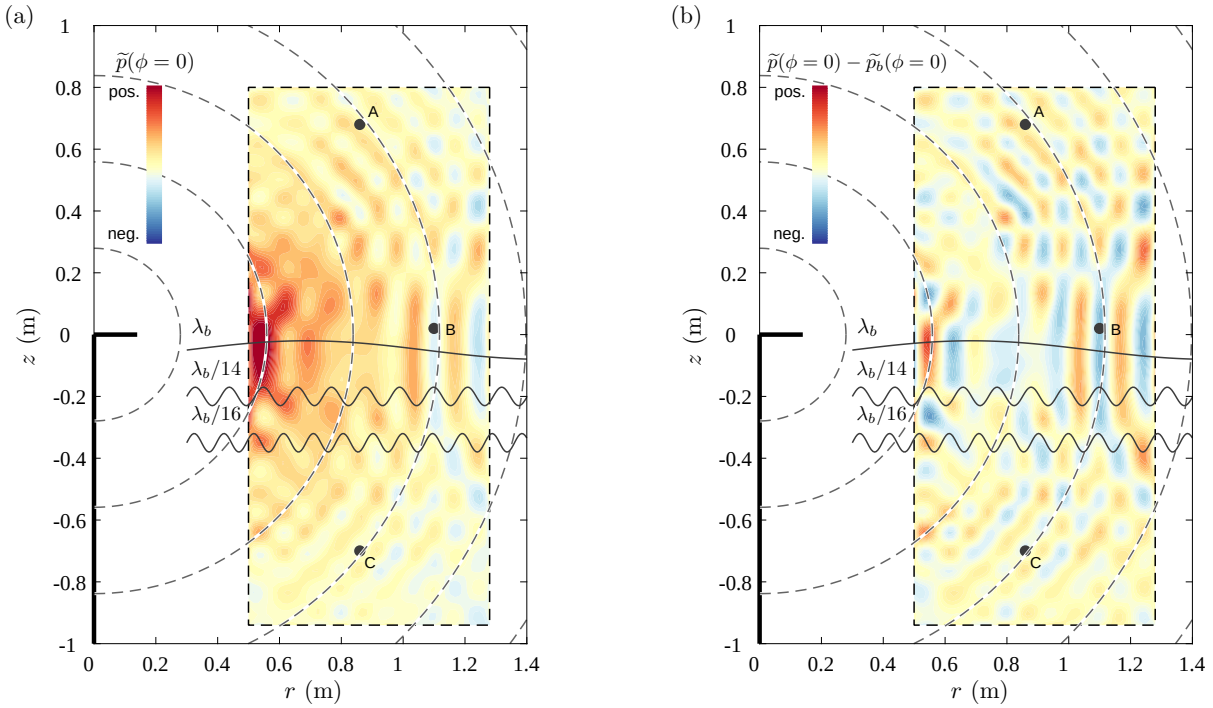

Figure 6. Spatial fields of the phase-averaged acoustic pressure for a blade position of $\phi = 0$; (a) was generated using the raw pressure data, while (b) is based on the pressure in the absence of the BPF tone at $f = f_b$. Spatial wavelengths of the primary BPF ($\lambda_b = a_\infty / f_b$) and its strongest harmonics (at $14 f_b$ and $16 f_b$, see Fig. 3b) are visualized for reference.

the rotor hub and that the red-colored region in Fig. 6a resembles the positive pressure fluctuation of the BPF tone (wavelengths are shown for ease of interpretation). The finer undulations within the acoustic field (particularly clear in Fig. 6b) survived the phase-average, and are thus *phase-locked* to the BPF; their wavelengths correspond to the 14^{th} and 16^{th} harmonic (postulated to be motor noise as discussed earlier). Due to spatial aliasing[55] however, the higher-frequency waves are distorted—the inter-microphone distance dictates a spatial Nyquist criterion. This does not influence our *temporal* modulation analysis (§ IV), as that is done per acoustic time series at a single point, similar to how the human ear perceives a temporal signal.

The phase-averaged pressure for one full rotation of the rotor, spanning $\phi = [0, 2\pi)$, is shown in Fig. 7 for positions A, B and C. Here p displays one ensemble (one blade rotation) of the raw pressure signal and constitutes harmonic and broadband noise. The phase-averaged pressure $\widetilde{p}$ comprises a clear signal of the blade passage (denoted as $\widetilde{p}_b$ and shown in red) with the superimposed periodic content resembling Fig. 6. This signal by itself (thus $\widetilde{p} - \widetilde{p}_b$) is modulated due to nonlinear interactions; we will further elaborate on this in § IV. Since the phase-averaging removes the (phase-inconsistent) broadband noise, we need to reside to methods other than phase-averaging, in order to assess the inter-frequency coupling of the BPF tone with the broadband noise content.

IV. Methodology of quantifying modulation

Our methodology of quantifying modulation (a strong *buzzing* character of the rotor noise) is applicable to a single acoustic time series. In this work we exclusively focus on how the BPF tone modulates the intensity of higher-frequency noise, although, when changing the modulating signal, the same methodology could in principle be used to research other 'drivers' of modulation. The diagram in Fig. 8 indicates that an

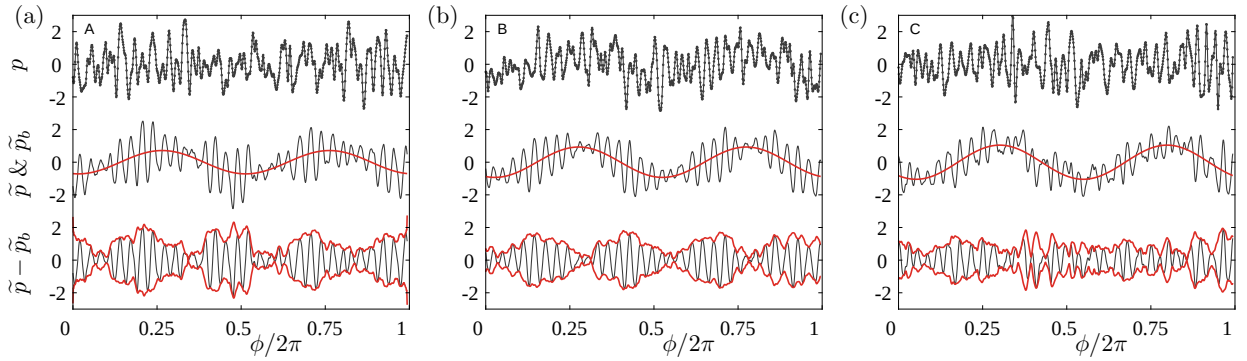

Figure 7. (a,b,c) Phase-averaged pressure at positions A, B and C as a function of one full rotation of the rotor. *Top:* one ensemble of the raw pressure p, *Middle:* phase-averaged pressure signal, $\widetilde{p}$, and the BPF tone $\widetilde{p}_b$ in red, *Bottom:* phase-averaged pressure signal (and envelope) in the absence of the BPF tone.

auto-bispectral analysis is the first step (detailed next in § IV.A). Next, in § IV.B, we discuss the details of how a modulation parameter is formed.

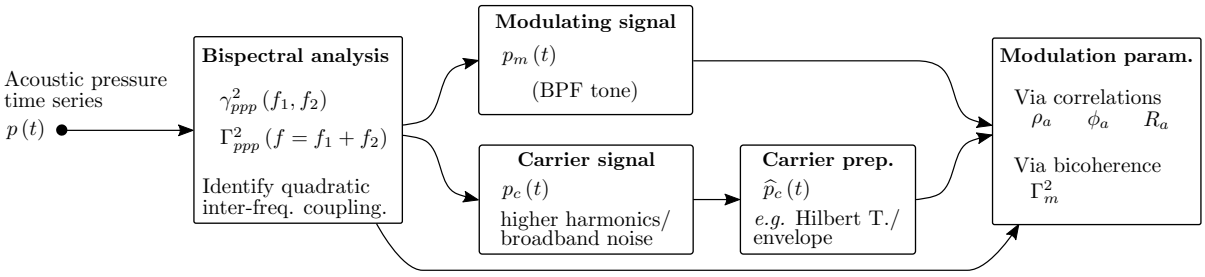

Figure 8. Flow diagram of the methodology to quantify modulation in a single acoustic pressure time series of small-scale rotor noise.

A. Bispectral analysis

By way of bispectral analysis we can examine the dominant nonlinear inter-frequency coupling, out of all possible frequency combinations present within a signal.[56,57] That is, bispectral analysis effectively correlates two frequency components to their sum (or difference). This type of spectral analysis thus assesses the *quadratic* frequency interactions, in which energetic content at frequencies f_1 and f_2 may be phase-coupled to (or interact with) the content at $f_3 = f_1 + f_2$ (f_1, f_2 and f_3 are said to form a triad). In the results of bispectral analysis we will confine ourselves to the auto-bicoherence spectrum, which is a normalized auto-bispectrum, following:

$$\gamma^2_{ppp} = \frac{|\phi_{ppp}(f_1, f_2)|^2}{\phi_{pp}(f_1)\,\phi_{pp}(f_2)\,\phi_{pp}(f_1 + f_2)}, \tag{2}$$

where the one-sided cross-bispectrum is taken as

$$\phi_{ppp}(f_1, f_2) = 2\langle P(f_1 + f_2)\,P^*(f_1)\,P^*(f_2)\rangle. \tag{3}$$

Recall that $P(f) = \mathcal{F}[p(t)]$ is the temporal FFT and that the position coordinates z and r are omitted for ease of notation. The angular brackets denote ensemble-averaging, performed with a similar resolution as for the spectral analysis carried out before. Since the auto-bicoherence is normalized by the auto-spectra, $\gamma^2_{ppp} \in [0, 1]$ and indicates the degree of normalized correlation between the energy at f_1 and f_2, and the energy at $f_1 + f_2$ (here we only consider sum-interactions, and not the difference-interactions per $f_3 = f_1 - f_2$, as we are interested in how the relatively low-frequency BPF modulates higher-frequency noise).

A contour of the auto-bicoherence is shown in Fig. 9a for $p(t)$ at position B. Note that the contour follows a logarithmic color scale via $\log_{10}\left[\gamma^2_{ppp}(f_1, f_2)\right]$, that the f_1 and f_2 axes are also logarithmic, and that the

(f_1, f_2) domain for which data is available comes forth from the fact that $f_3 = f_1 + f_2$ is bounded by the Nyquist frequency $f_N = f_s/2$. A ridge of relatively strong correlation, $\gamma^2_{ppp} \approx 0.1$, appears along $f_2 = f_b$, meaning that the BPF is phase-coupled to a broad range of frequencies $f_1 > f_b$ (the horizontal ridge). This is *direct evidence* that the BPF tone couples with the higher-frequency *broadband* content. This quadratic coupling is generally suppressed in phase averaging (§ III.B), as the *phase* in the bispectrum can still vary per triad. Other noticeable regions of interest in the auto-bicoherence include the point $(f_1, f_2) = (\omega, \omega)$ (the rotation rate causing a harmonic at the BPF via $f_b = \omega + \omega$ for the two-bladed rotor) and point $(f_1, f_2) = (f_b, \omega)$ (generating weak sum-interactions at $f_3 = 1.5 f_b$).

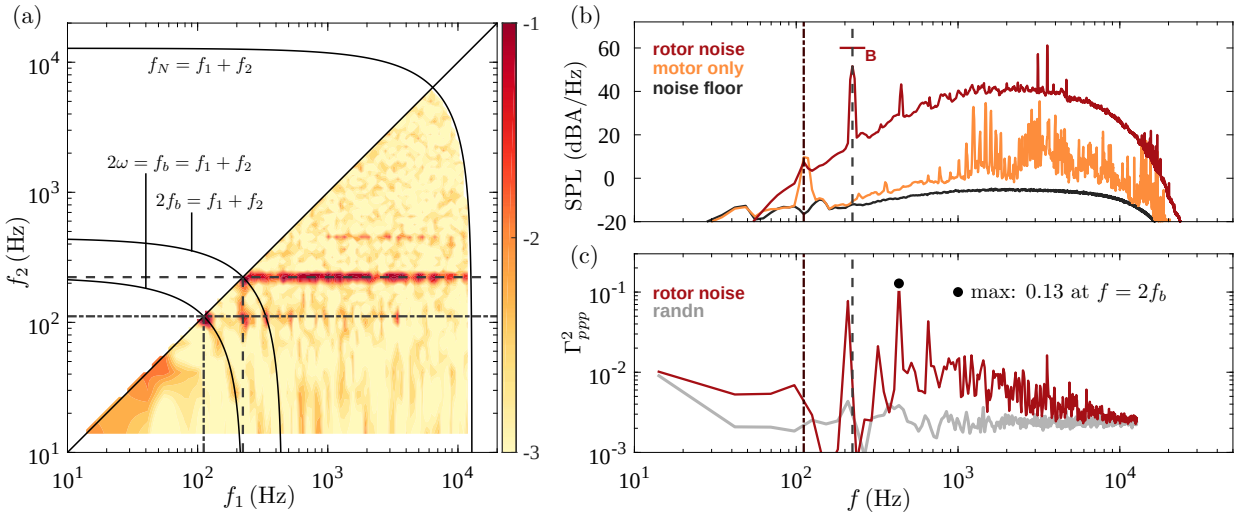

Figure 9. (a) Contour of the auto-bicoherence $\log_{10}\left[\gamma^2_{ppp}(f_1, f_2)\right]$ at position B. (b) Acoustic spectrum at position B (repeat from Fig. 3b), with alongside in (c) the summed auto-bicoherence $\Gamma^2_{ppp}(f = f_1 + f_2)$ for the rotor noise, and for a generated signal comprising random noise.

To infer what content in the auto-spectrum (Fig. 9b, a repeat of spectrum B in Fig. 3b) is involved in quadratic sum-interactions, we can condense the 2D auto-bicoherence $\gamma^2_{ppp}(f_1, f_2)$ to a summed bicoherence[58–60] by way of averaging along lines of constant $f = f_1 + f_2$:

$$\Gamma^2_{ppp}(f) = \frac{1}{N_q(f)} \sum_{f=f_1+f_2} \gamma^2_{ppp}(f_1, f_2)\,. \tag{4}$$

Here $N_q(f)$ is the number of frequency doublets f_1, f_2. This summed bicoherence spectrum is shown in Fig. 9c and its frequency axis is aligned with the auto spectrum in Fig. 9b. It is evident that Γ^2_{ppp} shows the degree of nonlinear interactions that are buried in certain frequency components (but for their f_1 and f_2 origin we would have to reside back to Fig. 9a). On a final note, the summed bicoherence spectrum is also plotted for a generated signal comprising random noise (uncorrelated in a linear and nonlinear way), highlighting that the bicoherence in the rotor noise signal is significant; it was furthermore ensured that all results of our bispectral analysis are converged.[46]

Given that the auto-bicoherence helps us form a holistic view on the degree of phase coupling, we can define a single metric when considering the BPF tone as one for the primary frequencies forming all possible quadratic frequency doublets. For this we take the mean value of the auto-bicoherence along $f_2 = f_b$, according to

$$\Gamma^2_m = \frac{1}{N_a} \sum_{f_1} \gamma^2_{ppp}(f_1, f_2 = f_b)\,. \tag{5}$$

Γ^2_m is a measure for the degree of phase coupling between the noise at $f > f_b$ and the BPF tone at $f = f_b$ (N_a is the number of discrete points over which the auto-bicoherence is summed). From a preliminary assessment of the auto-bicoherence and parameter Γ^2_m at positions A, B and C (Fig. 10), it is evident that Γ^2_m is varying in the field (*e.g.* Γ^2_m is minimum at position A and maximum at position B, when considering A, B and C only). Before we progress with a discussion of modulation trends in the rotor's acoustic field, we

proceed with the second part of the diagram in Fig. 8, in which the modulation is detailed via modulating- and carrier-signals.

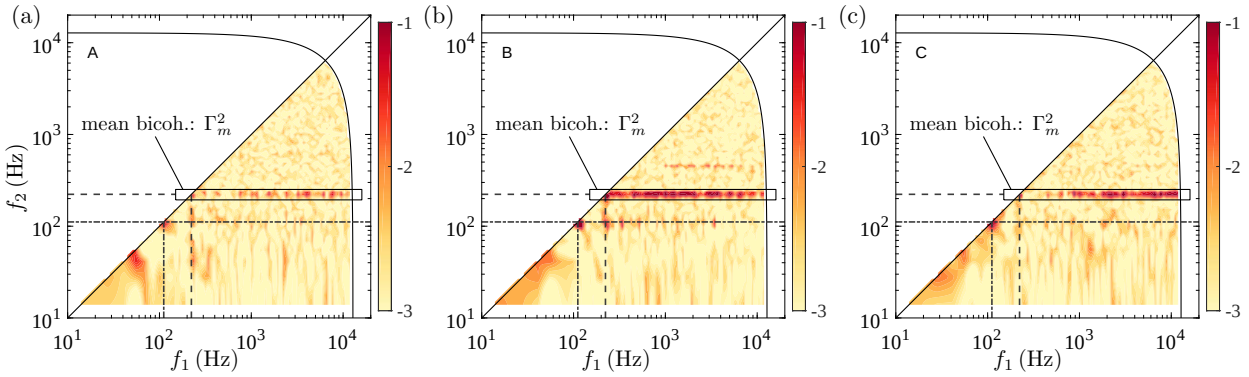

Figure 10. (a,b,c) Contours of the auto-bicoherence $\log_{10}\left[\gamma^2_{ppp}\left(f_1, f_2\right)\right]$ at positions A, B and C. The rectangular box encompassing $f_2 = f_b$ identifies the portion of the auto-bicoherence used in forming Γ^2_m.

B. Correlation of modulating and carrier signals

Since the bispectral analysis made apparent that the BPF tone is phase-coupled with the higher-frequency noise, we can proceed with detailing how the modulating signal (the BPF signature) influences a carrier signal. The *modulating signal* $p_b(t)$ is taken as the BPF tone. The raw acoustic time series $p(t)$ is plotted at the top of Fig. 11a in grey-scale, with the BPF tone $p_b(t)$ superimposed in red. The illustration is confined to 16 blade passages, but the statistical analyses are carried out for all $\sim$ 6680 blade passages. A carrier signal is one that is modulated by the modulating signal, here denoted as $p_h(t)$ (subscript h refers to the high-frequency content), and is taken as the high-pass filtered $p(t)$ with a cutoff frequency of $f = 1.75 f_b$; shown in grey-scale at the bottom of Fig. 11a. Cutoff $f = 1.75 f_b$ ensures that the carrier signal does not contain content of the triad formed by the one-per-revolution noise and the BPF signature, following $f = \omega + f_b = 1.5 f_b$. When assessing how this broadband noise is modulated, an envelope signal is first generated via a Hilbert transform $\widehat{p}_h(t) = |H[p_h(t)]|$ and superimposed in red (this prepares the carrier signal before it can be correlated with the modulating signal, see Fig.8). Figs. 11b and 11c are identical to 11a, but now for positions B and C, respectively. Note that especially the envelope signals of positions B and C show a degree of correlation with the BPF tones.

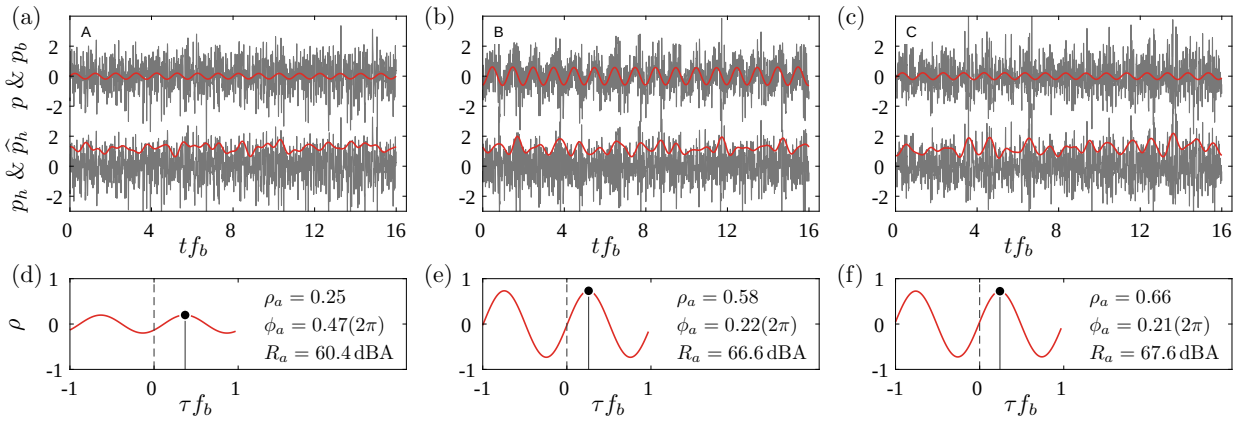

Figure 11. (a,b,c) Acoustic pressure at positions A, B and C over 16 blade passages. *Top:* raw pressure signal p and BPF signal p_b; *Bottom:* higher-frequency content pressure signal p_h ($f > 1.75 f_b$), together with envelope signal $\widehat{p}_h$. (d,e,f) Correlation of the modulating (p_b) and carrier signals ($\widehat{p}_h$) as a function of temporal lag τ. Modulation parameters are listed for each case.

All elements are now available for computing our modulation parameters. By (linearly) correlating the

modulating signal $p_b(t)$ with the carrier envelope $\widehat{p}_h$, we obtain temporal cross-correlation $R_a(\tau)$:

$$R(\tau) = \langle p_b(t)\, \widehat{p}_h(t-\tau) \rangle. \tag{6}$$

Subscript a refers to amplitude modulation and τ is the temporal lag. When normalizing with the standard deviations of the signals, the normalized correlation is obtained:

$$\rho(\tau) = \frac{R(\tau)}{\sigma(p_b)\,\sigma(\widehat{p}_h)}. \tag{7}$$

Figs. 11d,e,f plot the normalized correlations (which are harmonic due to the p_b signal being harmonic) and carries information on the strength of modulation, as well as the relative phase between the modulating and carrier signals. From the temporal correlations we define the modulation parameters as ρ_a, R_a and ϕ_a. The strength of the *normalized* modulation strength $\rho_a = \max[\rho(\tau)]$ is taken as the maximum of the normalized correlation (note $\rho_a \in [0,1]$); the *absolute* modulation strength $R_a = 10\log_{10}(\max[R(\tau)]/p^2_{\text{ref}})$ is the maximum of the dimensional correlation and is in dBA-scale; and finally $\phi_a = \tau f_b|_{\max[\rho(\tau)]}$ is the relative phase between the signals of maximum correlation, in radians. All modulation parameters ρ_a, R_a and ϕ_a, as well as the Γ^2_m metric of the bispectral analysis, are computed for each of the 420 acoustic signals of the grid measurements; results are discussed next.

V. Results of acoustic modulation

Spatial fields of the normalized modulation strength $\rho_a(z,r)$ and the auto-bicoherence-based metric $\Gamma^2_m(z,r)$ are shown in Figs. 12a and 12b, respectively. Notably, ρ_a indicates that modulation is primarily confined to a sector $\theta \approx (10°, -45°)$, where $\theta = 0°$ is the rotor plane and negative angles are in the downstream direction. The acoustic modulation is dictated by the rotor blade's higher-frequency noise

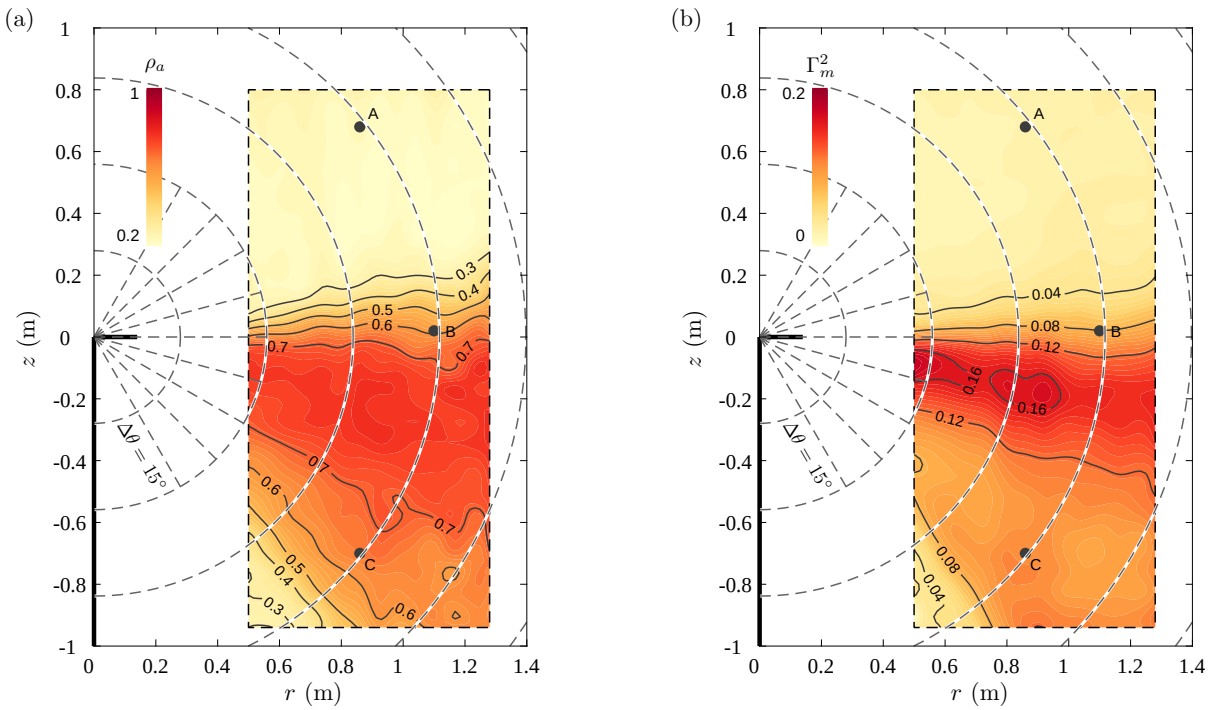

Figure 12. Spatial fields of (a) the normalized modulation strength ρ_a and (b) the auto-bicoherence-based metric Γ^2_m. Modulation is strongest in the sector $\theta \approx (10°, -45°)$ (sideline and downstream regimes) and, in a normalized sense, appears to be constant with outward distance.

sources that advance and retreat, depending on the blade's phase. Furthermore, the normalized modulation strength remains constant with outward distance (and the same for the modulating-carrier phase, presented in Fig. 13b), showing that the sound propagation of the phase coupled content is non-dispersive. Parameter

Γ_m^2 is a direct measure of the efficacy at which the BPF tone is coupled with the higher-frequency noise content. Generally this contour indicates the same region where there is a significant coupling, but the ridge of maximum Γ_m^2 aligns closer to the rotor disk plane at around $\theta \approx -10°$. It is important to realize that Γ_m^2 is derived from the magnitude of the auto-bicoherence (and does not include phase information of the underlying auto-bispectrum). As such, the strength of BPF modulation in the classical sense (a buzzing/breathing of higher-frequency noise at a rate of the BPF) is believed to be better quantified by ρ_a. That is, ρ_a implicitly preserved the phase of the frequency content in the 'total' carrier signal, while Γ_m^2 is a measure of the phase-coupling on a per-frequency basis.

Two final contours of the absolute modulation strength $R_a(z, r)$, and the relative phase $\phi_a(z, r)$ between the modulating and carrier signal, are shown in Figs. 13a and 13b, respectively. As expected, R_a shows a similar spatial trend as ρ_a, but the contour is now weighted with the energy present in both the BPF signature and high-frequency content (see discussion of Figs. 5b and 5c). A strong buzzing character of the rotor noise will thus be apparent, most distinguishable around $\theta \approx -20°$, and even though the total acoustic pressure amplitude decays in the far-field, the relative strength of the buzzing tone remains constant with outward distance per Fig. 12a. Interestingly, the region of minimum modulation ($\theta > 10°$ and $\theta < -45°$) is, in addition, also characterized by an out-of-phase behavior of the modulating and carrier signals since $\phi_a \approx 0.5(2\pi)$ (note that the out-of-phase behavior is not a cause for the smaller modulation strength, as the modulation strength was always determined by the maximum of the correlation curve).

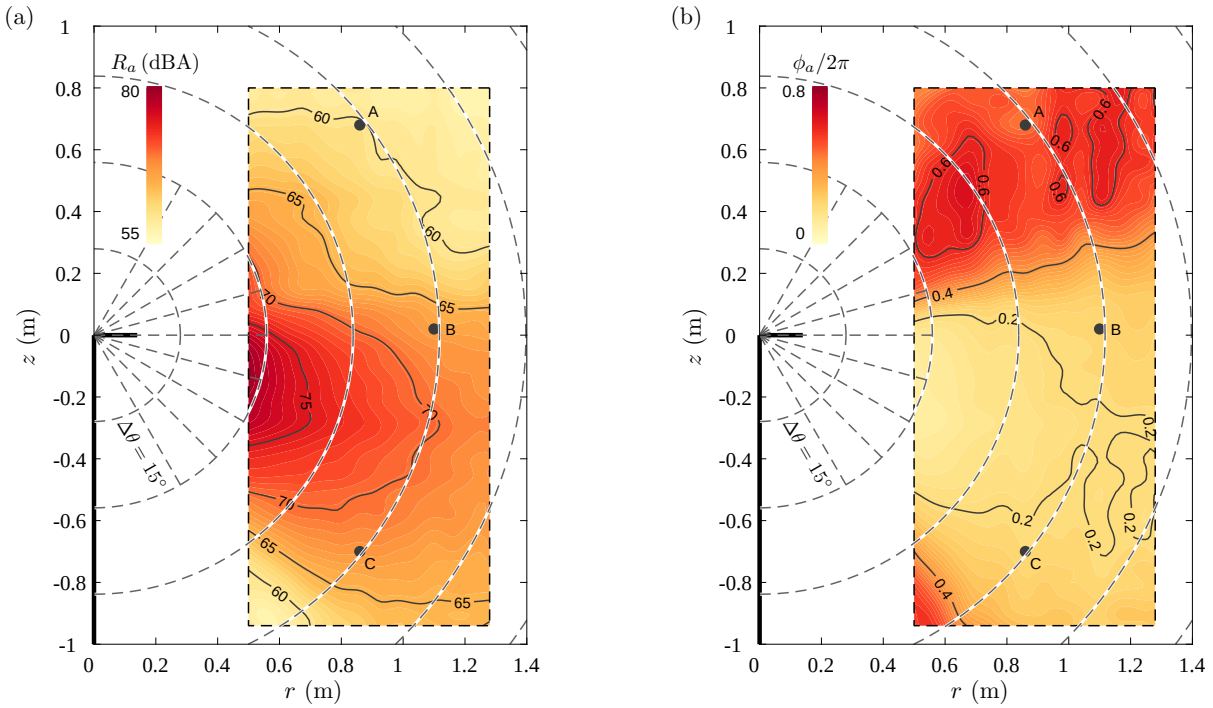

Figure 13. Spatial fields of (a) the absolute modulation strength R_a and (b) the phase between the modulation and carrier signals at which the maximum correlation occurs. Outside the sector of strong modulation—θ outside the range $(10°, -45°)$—the weak modulation ($\rho_a \leq 0.2$, Fig. 12a) coincides with an out-of-phase behavior of the modulating and carrier signals ($\phi_a \approx 0.5(2\pi)$).

VI. Concluding remarks

This work has presented a methodology for quantifying modulation in the acoustic field generated by a small-scale rotor in hover. The modulation of interest is concerned with the periodic advance and retreat of the rotor blade's noise sources, at a rate that is equal to the BPF. Modulation parameters relied on correlation-based techniques, between a modulating signal (BPF signature) and a carrier signal comprising higher-frequency noise. Acoustic time series at 420 microphone positions in the acoustic near- and far-fields of the rotor allowed for a visualization of spatial trends of the modulation strength. A few concluding remarks

are provided as follows:

(i) Extensive acoustic measurements in the near- and far-field of the small-scale rotor in hover revealed that the acoustic far-field of the BPF signature starts, at least, beyond $r \sim 5D_p$ from the rotor hub (this is expected since two wavelengths of the BPF in this study corresponds to $\sim 11D_p$). Nevertheless, future measurements should reveal the far-field characteristics of the BPF signature such as its directivity.

(ii) The pressure amplitude of the higher frequency noise content (here considered as $f > 5f_b$) was found to obey spherical decay from our closest measurement at the source at $r \approx 1.8D_p$. This suggests that these noise sources are very compact as the far-field starts at a distance from the rotor-hub of less than 2 wavelengths.

(iii) Correlation-based metrics were successfully applied to acoustic time series to quantify inter-frequency modulation. Preliminary listening experiments revealed that the modulation strength-parameters are well-correlated with the degree of time-variation of the amplitude. Future work is needed to correlate this engineering parameter to human perception and annoyance via psycho-acoustic methods. When successful, the current methodology could be a promising post-processing scheme to address noise annoyance factors of advanced air mobility vehicles and drones.

(iv) Our analysis revealed that modulation in the case of a small-scale rotor in hover is primarily confined to a sector $\theta \approx (10°, -45°)$, where $\theta = 0°$ is the rotor plane and negative angles are in the direction of the rotor-induced flow. The ridge of maximum modulation appears around $\theta \approx -20°$.

Acknowledgements

We wish to gratefully acknowledge SBIRD ID8868-414480 for financial support and the insight provided by its program manager Alex Skvortsov. The project was completed in partnership with XROTOR PTY LTD. We would also like to give special thanks to Geoff Durham, Ken King, Dean Sutcliffe, Ryan Pope, James Gumley, Robert Carrese, Pier Marzocca and Simon Watkins for technical discussions and to Domenico Tedesco and Huw James for their development of the experimental rig. Experiments were made possible by Christopher Preston and John Davy of CSIRO (Clayton, Australia), by generously making their anechoic chamber available. This research was undertaken as part of the RMIT Unmanned Aircraft Systems Research Team, within the Sir Lawrence Wackett Aerospace Research Centre, at RMIT University.

References

[1]Tegler, J., "Noise alert!" *Aerospace America, AIAA*, Vol. 58, No. 4, 2020.

[2]Christian, A. and Cabell, R., "Initial investigation into the psychoacoustic properties of small unmanned aerial system noise," *AIAA Paper 2017-4051*, 2017.

[3]Rizzi, S. A., Palumbo, D. L., Rathsam, J., Christian, A. W., and Rafaelof, M., "Annoyance to noise produced by a distributed electric propulsion high-lift system," *AIAA Paper 2017-4050*, 2017.

[4]Zawodny, N. S. and Pettingill, N. A., "Acoustic wind tunnel measurements of a quadcopter in hover and forward flight conditions," *INTER-NOISE 2018*, Chicago, IL, Aug. 2018.

[5]Krishnamurthy, S., Christian, A., and Rizzi, S. A., "Psychoacoustic test to determine sound quality metric indicators of rotorcraft noise annoyance," *INTER-NOISE 2018*, Chicago, IL, Aug. 2018.

[6]Christian, A., Caston, J., and Greenwood, E., "Regarding the perceptual significance and characterization of broadband components of helicopter source noise," *Vertical Flight Society 75th Annual Forum*, Philadelphia, PA, May 2019.

[7]Yang, Y., Liu, Y., Li, Y., and Arcondoulis, E., "Aerodynamic and aeroacoustic performance of an isolated multicopter rotor during forward flight," *AIAA J.*, Vol. 58, No. 3, 2020, pp. 1171–1181.

[8]Fastl, H. and Zwicker, E., *Psychoacoustics: facts and models*, Springer-Verlag, New York, 2007, Chapter 10, Fluctuation strength, pp. 247256.

[9]Ol, M., Zeune, C., and Logan, M., "Analytical – experimental comparison for small electric unmanned air vehicle propellers," *AIAA Paper 2008-7345*, 2008.

[10]Brandt, J. B. and Selig, M. S., "Propeller performance data at low Reynolds numbers," *AIAA Paper 2011-1255*, 2011.

[11]Sinibaldi, G. and Marino, L., "Experimental analysis on the noise of propellers for small UAV," *J. Applied Acoust.*, Vol. 74, No. 1, 2013, pp. 79–88.

[12]Zawodny, N. S., Boyd Jr., D. D., and Burley, C. L., "Acoustic characterization and prediction of representative, small-scale rotary-wing unmanned aircraft system components," *American Helicopter Society 72nd Annual Forum*, West Palm Beach, FL, May 2016.

[13]Zawodny, N. S. and Boyd Jr., D. D., "Investigation of rotor-airframe interaction noise associated with small-scale rotary-wing unmanned aircraft systems," *American Helicopter Society 73rd Annual Forum*, Fort Worth, TX, May 2017.

[14]Tinney, C. E. and Sirohi, J., "Multirotor drone noise at static thrust," *AIAA J.*, Vol. 56, No. 7, 2018, pp. 2816–2826.

[15]Tinney, C. E. and Valdez, J., "Acoustic scaling for small rotors in hover," *Vertical Flight Society 75th Annual Forum*, Philadelphia, PA, May 2019.

[16]Jordan, W., Narsipur, S., and Deters, R. W., "Aerodynamic and aeroacoustic performance of small UAV propellers in static conditions," *AIAA Paper 2020-2595*, 2020.

[17]Stephenson, J. H., Tinney, C. E., Greenwood, E., and Watts, M. E., "Time frequency analysis of sound from a maneuvering rotorcraft," *J. Sound Vibr.*, Vol. 333, 2014, pp. 5324–5339.

[18]Rizzi, S. A., Zawodny, N. S., and Pettingill, N. A., "On the use of acoustic wind tunnel data for the simulation of sUAS flyover noise," *AIAA Paper 2019-2630*, 2019.

[19]Janssen, S. A., Eissen, A. R., and Pedersen, E., "Exposure-response relationships for annoyance by wind turbine noise: a comparison with other stationary sources," *EURONOISE 2009*, Edinburgh, Scotland, Oct. 2009.

[20]Bockstael, A., Dekoninck, L., de Coensel, B., Oldoni, D., Can, A., and Botteldooren, D., "Wind turbine noise: annoyance and alternative exposure indicators," *Forum Acusticum 2011*, Aalborg, Denmark, July 2011.

[21]Lee, S., Kim, K., Choi, W., and Lee, S., "Annoyance caused by amplitude modulation of wind turbine noise," *Noise Control Eng. J.*, Vol. 59, No. 1, 2011, pp. 38–46.

[22]Nguyen, P. D., Hansen, K. L., and Zajamsek, B., "Characterizing tonal amplitude modulation of wind farm noise," *Acoustics 2018*, Adelaide, Australia, Nov. 2018.

[23]Gerard, A., Moreau, S., Berry, A., and Masson, P., "Acoustic modulation effect of rotating stator/rotor interaction noise," *Acoustics 2012*, Nantes, France, April 2012.

[24]Marte, J. E. and Kurtz, D. W., "A review of aerodynamic noise from propellers, rotors, and lift fans," NASA/TR-32-1462, NASA, 1970.

[25]Amiet, R. K., "Noise produced by turbulent flow into a propeller or helicopter rotor," *AIAA J.*, Vol. 15, No. 3, 1977, pp. 307–308.

[26]Glegg, S. and Devenport, W., *Aeroacoustics of low Mach number flows*, Academic press, Elsevier, Amsterdam, Netherlands, 2017, Chapter 16, Open rotor noise, pp. 399-436.

[27]Candeloro, P., Pagliaroli, T., Ragni, D., and Di Francesco, S., "Small-scale rotor aeracoustics for drone propulsion: a review of noise sources and control strategies," *Preprints*, 2019, 2019100078.

[28]Rizzi, S. A., Huff, D. L., Boyd Jr., D. D., Bent, P., Henderson, B. S., Pascioni, K. A., Sargent, D. C., Josephson, D. L., Marsan, M., He, H., and Snider, R., "Urban Air Mobility noise: current practice, gaps, and recommendations," NASA/TR-32-1462, NASA, 2020.

[29]Henricks, Q., Wang, Z., and Zhuang, M., "Small-scale rotor design variables and their effects on aerodynamic and aeroacoustic performance of a hovering rotor," *J. Fluids Eng.*, Vol. 142, No. 081209, 2020, pp. 1–13.

[30]Lee, H. and Lee, D., "Rotor interactional effects on aerodynamic and noise characteristics of a small multirotor unmanned aerial vehicle," *Phys. Fluids*, Vol. 32, 2020, 047107.

[31]Casalino, D., van der Velden, W. C. P., and Romani, G., "Community noise of urban air transportation vehicles," *AIAA Paper 2019-1834*, 2019.

[32]Casalino, D., van der Velden, W. C. P., Romani, G., and Gonzales-Martino, I., "Aeroacoustic analysis of urban air operations using the LB/VLES method," *AIAA Paper 2019-2662*, 2019.

[33]Whiteside, S., Zawodny, N., Fei, X., Pettingill, N. A., Patterson, M. D., and Rothaar, P., "An exploration of the performance and acoustic characteristics of UAV-scale stacked rotor configurations," *AIAA Paper 2019-1071*, 2019.

[34]McKay, R. S., Kingan, M. J., and Go, R., "Experimental invesitgation of contro-rotating multi-rotor UAV propeller noise," *Proceedings of ACOUSTICS 2019*, Cape Schanck, VIC, Australia, Nov. 2019.

[35]Tinney, C. E. and Valdez, J., "Thrust and acoustic performance of small-scale, coaxial, corotating rotors in hover," *AIAA J.*, Vol. 58, No. 4, 2020, pp. 1657–1667.

[36]Pascioni, K. A., Rizzi, S. A., and Schiller, N. H., "Noise reduction potential of phase control for distributed propulsion vehicles," *AIAA Paper 2019-1069*, 2019.

[37]Krishnamurthy, S. and Rizzi, S. A., "Auralization of amplitude modulated helicopter flyover noise," *AIAA Paper 2019-2087*, 2019.

[38]Bian, H., Fattah, R., Sun, Y., and Zhang, X., "Noise prediction of drones in urban environments," *AIAA Paper 2019-2685*, 2019.

[39]Han, D., Gwak, D. Y., and Lee, S., "Noise prediction of multi-rotor UAV by RPM fluctuation correction method," *J. Mech. Sci. Techn.*, Vol. 34, No. 4, 2020, pp. 1429–1443.

[40]Roger, M. and Moreau, S., "Tonal-noise assessment of quadrotor-type UAV using source-mode expansions," *Acoustics*, Vol. 2, 2020, pp. 674–690.

[41]Li, S. and Lee, S., "A machine learning-based fast prediction of rotorcraft broadband noise," *AIAA Paper 2020-2588*, 2020.

[42]Stephenson, J. H., Weitsman, D., and Zawodny, N. S., "Effects of flow recirculation on unmanned aircraft system (UAS) acoustic measurements in closed anechoic chambers (L)," *J. Acoust. Soc. Am.*, Vol. 145, No. 3, 2019, pp. 11531155.

[43]Viswanathan, K., "Instrumentation considerations for accurate jet noise measurements," *AIAA J.*, Vol. 44, No. 6, 2006, pp. 1137–1149.

[44]Fiévet, R., Tinney, C. E., Baars, W. J., and Hamilton, M. F., "Coalescence in the sound field of a laboratory scale supersonic jet," *AIAA J.*, Vol. 54, No. 1, 2016, pp. 254–265.

[45]Cambray, A., Pang, E., Showkat Ali, S. A., Rezgui, D., and Azarpeyvand, M., "Investigation towards a better understanding of noise generation from UAV propellers," *AIAA Paper 2018-3450*, 2018.

[46]Poloskei, P. Z., Papp, G., Por, G., Horvath, L., and Pokol, G. I., "Bicoherence analysis of nonstationary and nonlinear processes," *arXiv:1811.02973 [eess.SP]*, 2018.

[47]Deters, R. W., Ananda, G. K., and Selig, M. S., "Reynolds number effects on the performance of small-scale propellers," *AIAA Paper 2014-2151*, 2014.

[48]Serré, R., Gourdain, N., Jardin, T., Jacob, M. C., and Moschetta, J., "Towards silent micro-air vehicles: optimization of a low Reynolds number rotor in hover," *Int. J. Aeroacoustics*, Vol. 18, No. 8, 2020, pp. 690–710.

[49]Baars, W. J., Tinney, C. E., Wochner, M. S., and Hamilton, M. F., "On cumulative nonlinear acoustic waveform distortions from high-speed jets," *J. Fluid Mech.*, Vol. 749, 2014, pp. 331–366.

[50]Fletcher, H. and Munson, W. A., "Loudness, its definition, measurement and calculation," *J. Acoust. Soc. Am.*, Vol. 5, 1933, pp. 82–108.

[51]Huff, D. L. and Henderson, B. S., "Electric motor noise for small quadcopters: Part 1 – Acoustic measurements," *AIAA Paper 2018-2952*, 2018.

[52]Henderson, B. S., Huff, D., Cluts, J., and Ruggeri, C., "Electric motor noise for small quadcopters: Part II – Source characteristics and predictions," *AIAA Paper 2018-2953*, 2018.

[53]Yauwenas, Y., Fischer, J., Moreau, D., and Doolan, C., "The effect of inflow disturbance on drone propeller noise," *AIAA Paper 2019-2663*, 2019.

[54]Brentner, K. S. and Farassat, F., "Modeling aerodynamically generated sound of helicopter rotors," *Progr. Aerosp. Sci.*, Vol. 39, 2003, pp. 83–120.

[55]Scholte, R., Roozen, B., and Lopez, I., "On spatial sampling and aliasing in acoustic imaging," *12th ICSV*, Lisbon, Portugal, July 2015.

[56]Nikias, C. L. and Raghuveer, M. R., "Bispectrum Estimation: A Digital Signal Processing Framework," *Proceedings of the IEEE*, Vol. 75, No. 7, July 1987, pp. 869–890.

[57]Nikias, C. L. and Petropulu, A. P., *Higher-Order Spectra Analysis - A Nonlinear Signal Processing Framework*, PTR Prentice Hall, Englewood Cliffs, New Jersey, 1993.

[58]Boashash, B., Powers, E. J., and Zoubir, A. M., *Higher-Order Statistical Signal Processing*, Longman, Australia, 1995.

[59]Powers, E. J. and Im, S., "Introduction to Higher-Order Statistical Signal Processing and Its Applications," The University of Texas at Austin, Dept. of Electrical and Computer Engineering, Austin, Texas 78712-1084, Jan. 2004, *(document is an expanded version of ref. 58)*.

[60]Baars, W. J. and Tinney, C. E., "Proper orthogonal decomposition-based spectral higher-order stochastic estimation," *Phys. Fluids*, Vol. 26, 2014, 055112.